Cohesive failure analysis of an array of IC chips bonded to a stretched substrate

Zunxu Liu, Paolo S. Valvo, YongAn Huang, Zhouping Yin

PII: S0020-7683(13)00271-0
DOI: http://dx.doi.org/10.1016/j.ijsolstr.2013.06.021
Reference: SAS 8044

To appear in: *International Journal of Solids and Structures*

Received Date: 22 March 2013
Revised Date: 13 June 2013

Please cite this article as: Liu, Z., Valvo, P.S., Huang, Y., Yin, Z., Cohesive failure analysis of an array of IC chips bonded to a stretched substrate, *International Journal of Solids and Structures* (2013), doi: http://dx.doi.org/10.1016/j.ijsolstr.2013.06.021

Cohesive failure analysis of an array of IC chips bonded to a stretched substrate

Zunxu Liu[a], Paolo S. Valvo[b], YongAn Huang[a,*], Zhouping, Yin[a,*]

[a] *State Key Laboratory of Digital Manufacturing Equipment and Technology, Huazhong University of Science and Technology, Wuhan, 430074, China*

[b] *Department of Civil and Industrial Engineering, University of Pisa, Largo Lucio Lazzarino, I-56126 Pisa, Italy*

Abstract

The paper presents a mechanical model for predicting the cohesive failure of a periodic array of integrated circuit (IC) chips adhesively bonded to a stretched substrate. A unit cell of the layered structure consisting of the IC chips, adhesive layer, and substrate is modeled as an assembly of two elastic Timoshenko beams, representing the chip and substrate, connected by an elastic interface, representing the adhesive. Accordingly, the stresses and energy release rate (ERR) in the adhesive layer – responsible for the premature cracking of the adhesive and debonding of the IC chips – are identified with the corresponding quantities computed for the elastic interface. Expressions for the adhesive stresses and ERR are given in terms of geometrical dimensions and material properties, combined with integration constants obtained numerically via the multi-segment analysis method. For comparison, the stresses in the adhesive are also computed based on a finite element model, and the ERR is evaluated using the virtual crack-closure technique (VCCT). The analytical predictions and numerical results match fairly well, considering the effects of key factors, such as the distance between adjacent chips, the chip size, the material properties of adhesive and substrate. The interaction between the chips is shown to have relevant effects on the adhesive stresses. In particular, only the mode II contributes to the ERR which increases with the ratio of the chip size to the distance between the chips and with the compliance of the adhesive and substrate layers.

* Corresponding authors.

Tel: +8613545354545; fax: +86 27 87543072.

E-mail address: yahuang@hust.edu.cn (YongAn Huang), yinzhp@mail.hust.edu.cn (Zhouping Yin).

Keywords: Fracture mechanics; Adhesive stresses; Debonding analysis; Adhesive layer; Energy release rate.

1. Introduction

Arrays of integrated circuit (IC) chips adhesively bonded to stretched substrates have found extensive applications in the field of flexible electronics and biosensor manufacturing, where large scale thin film transistor (TFT) arrays on flexible substrates are widely employed (Ko et al., 2008). The chip-on-substrate structure is a typical three layer framework consisting of chips, adhesive and substrate. Such multilayer structures are put in tension during typical manufacturing processes – such as the roll-to-roll and chip pick-up processing –, where the substrate is normally subjected to a fixed prestrain (Huang et al., 2011; Peng et al., 2011). However, an excess of prestrain may lead to high stress concentrations at the free edges of the bonding interfaces, which in turn may cause premature cracking of the adhesive and debonding of the IC chips (Feng and Wu, 2001; Park et al., 2008). Moreover, adjacent chips can interact with each other, thus promoting further debonding of the chips from the substrate. In the context of fracture mechanics, the aforementioned failure modes can be predicted based on the values of the stresses and energy release rate (ERR) in the adhesive layer and in the chip-on-substrate bond interfaces. Therefore, accurate modeling and efficient solution for reliable estimation of the adhesive stresses and ERR are of utmost importance for the design and manufacturing of flexible/stretchable electronics.

Several approaches to evaluate the stresses and ERR at the bond adhesive interface/layer have been proposed in the literature, including analytical solutions and numerical methods. In the earliest analytical studies, all layers are modeled as elastic beams or plates (da Silva et al., 2009). For two-layered/sandwich beams under axial, bending moments, transverse shear forces, or thermal loads, the mode I and II ERR contributions of steady state debonding and convergent debonding can be calculated using the complex variable method or the stress-function variational method (Hutchinson and Suo, 1992; He et al., 1997; Li et al., 2004; Qiao and Wang, 2004; Wang and Zhang, 2009; Lu et al., 2007). Among the cited studies, Lu et al. (2007) obtained an approximate expression for the ERR of a periodic array of islands debonding from a very compliant substrate. Especially for adhesively-bonded/composite joints, a number of analytical models have been

proposed over the past few decades (Goland and Reissner, 1944; Tsai et al., 1998; Wang et al., 2000; Luo and Tong, 2004, 2009; Bennati et al., 2009; Shahin and Taheri, 2008; Yang and Pang, 1996; Wang and Qiao, 2004; Chadegani et al., 2011, 2012). To obtain a closed-form solution, the adhesive layer is often modeled as a continuous distribution of linear tension/compression and shear springs. The adhesive layer is assumed to be very thin compared with the adherends, so that the peel and shear stresses in the adhesive layer exhibit no variation through the adhesive thickness. In this case, the governing differential equations can be deduced by adopting the adhesive stresses as the main unknowns. The pioneering work by Goland and Reissner (1944) furnished the classical solution in the stress analysis of adhesively bonded joints, and was improved by Tsai et al. (1998) to account for the adherend shear deformation. Wang et al. (2000) modeled all layers as Euler-Bernoulli beams and supplied an approximate closed-form solution for the adhesive peel and shear stresses in trilayer electronic assemblies based on the method of singular perturbation. Based on Timoshenko's beam theory, Luo and Tong (2009) obtained closed-form formulas for calculating the mode I and II ERR contributions for a straight interlaminar crack in a composite laminate. Bennati et al. (2009) developed a mechanical model where two Timoshenko beams are connected by a two-parameter elastic interface, which can be used to analyze the mixed-mode fracture of adhesive joints, composite laminates, and general layered structures. Other researchers used the first-order shear deformation plate theory (FSDT). Yang and Pang (1996, 2008) and Chadegani et al. (2011, 2012) presented an analytical model for determining the ERR for a crack in an adhesively-bonded composite joint with thin bondlines, where the governing equations were derived and solved using a Fourier series. Then, continuity and boundary conditions were used to evaluate the integration constants. The FSDT was also adopted by Wang and Qiao (2004) to model composite structures.

Moving on to numerical methods, the finite element method (FEM) is commonly adopted to calculate the stresses and ERR at the bond interface or adhesive layer. Most frequently, the ERR is evaluated using the virtual crack-closure technique (VCCT) based on the results of finite element analysis (FEA) (Camanho and Davila, 2002). The advantages of the VCCT include insensitivity to mesh size, no need to employ special crack tip elements and computational effectiveness with no more than two steps of analysis (Krueger, 2004), so that it has been considered as an indispensable methodology to obtain ERR and introduced into general use, e.g., Yang et al. (1996, 2008), Chadegani et al. (2011, 2012), Peng et al. (2011, 2012) etc. On the other hand, particular attention

should be paid when the VCCT is utilized in problems with bi-material interface cracks (Agrawal and Karlsson, 2006) or highly asymmetric cracks (Valvo, 2012). Xie and Biggers (2006, 2007) developed a new kind of interface element called fracture element with dummy nodes, for VCCT approach, through which the ERR can be calculated simultaneously as the FEA is performed.

The choice of the most appropriate solution method mainly depends on the particular problem being analyzed, such as the peeling of electronic packaging (Peng et al., 2011, 2012), the picking and placing of laser transfer printing (Li et al., 2012), or the delamination of composite laminates (Wang and Qiao, 2004). Yet, no standard solution strategy has been defined in the literature to analyze the problem of an array of IC chips periodically bonded to a stretched substrate. In this paper, we follow both the analytical and numerical approaches to investigate the adhesive stresses and debonding behavior of this particular layered structure. The layout of the paper is as follows. A mechanical model of the chip-on-substrate structure is presented in Section 2, whereby the governing differential equations are deduced. Section 3 describes the adopted solution strategy, with particular attention on showing how to apply the boundary and continuity conditions to obtain the integration constants involved in the analytical expressions of adhesive stresses. Furthermore, numerical results are presented and discussed in order to verify the accuracy of the analytical solution and investigate the distribution of the adhesive stresses. Lastly, Section 4 presents computational formulas for the mode II ERR for the periodic chip-on-substrate structure, which are used to analyze the influence of several parameters, such as the distance between adjacent chips, chip size, material properties of adhesive and substrate.

2. Analytical model

2.1. Mechanical model

We consider the chip-on-substrate structure consisting of a periodic array of chips adhesively bonded to a stretched substrate, illustrated in Fig.1(a). In consideration of the periodicity, the mechanical model can be restricted to a unit cell of length $2(l_1 + l_2)$, where $2l_1$ is the length of a single chip and l_2 is the half distance between two adjacent chips, as shown in Fig.1(b). Furthermore, thanks to the symmetry of the unit cell and external loading, calculations can be limited to the right-hand half portion of the unit cell, see Fig.1(c). The thicknesses of the chip and substrate are denoted by H_1 and H_2, respectively, and the thickness of the adhesive layer in between is h_a, with $h_a << H_1$, H_2. The materials are assumed to be linearly elastic and isotropic, and the corresponding

elastic moduli and Poisson's ratios are E_1, ν_1, E_2, ν_2, and E_a, ν_a for the chip, the substrate and the adhesive layer, respectively. A tensile load (per unit area), P, is applied along the axial direction to the right-hand end section of the substrate. It is assumed that a crack will initiate from the free end of the adhesive layer and propagate along its mid-plane.

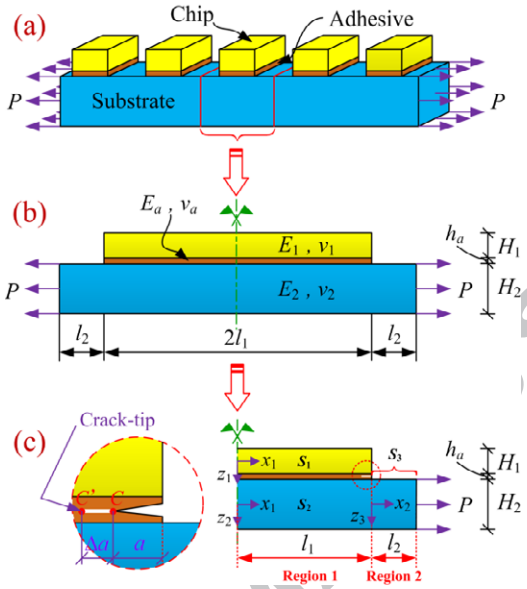

Fig.1. (a) Scheme of the periodic array of chips bonded to the substrate, subjected to uniaxial uniform traction; (b) plane strain model of the unit cell; (c) reduced right-hand half portion of the unit cell with a detail of the crack tip.

As depicted in Fig.1(c), starting from the symmetry axis, the body is divided into two regions, labeled as Region 1 and Region 2, with lengths l_1 and l_2, respectively. Furthermore, we define three segments: S_1, corresponding to the chip; S_2 and S_3, respectively corresponding to the portions of the substrate belonging to Regions 1 and 2. Local reference axes x_1 and x_2 measure the distance in the axial direction from left-hand end sections of Regions 1 and 2, respectively. Likewise, local axes z_1, z_2 and z_3 denote the distances in the transverse direction from the mid-planes of segments S_1, S_2 and S_3, respectively. Thus, for the generic segment S_i (i = 1, 2, 3), we have a local coordinate system, x_j, y_i, z_i (here, and in the following, j = 1, 2 represents Region 1 and 2, respectively), with the origin at the midpoint of the left edge of the segment. Each segment is modeled as an elastic beam according to Timoshenko's theory. Accordingly, we will derive the governing equations and couple them to each other by suitable continuity conditions, using the so-called multi-segment analysis method

which has been successfully used by other authors, e.g. Yang et al. (1996, 2008), and Chadegani et al. (2011, 2012) etc.

For each segment, N_i, Q_i, and M_i respectively denote the axial force, shear force, and bending moment per unit width. Furthermore, u_i^{o} and w_i indicate the segments' mid-plane displacements along the axial and transverse directions, respectively, and ϕ_i indicates the rotations of their cross sections. Correspondingly, $A_k = E_k^* H_k$, $C_k = k_s G_k H_k$, and $D_k = E_k^* H_k^3/12$ respectively are the extensional stiffness, shear stiffness, and bending stiffness of the chip ($k = 1$) and the substrate ($k = 2$) layers. Here, $E_k^* = E_k / (1 - \nu_k^2)$ and $G_k = E_k / [2(1 + \nu_k)]$ are the effective Young's modulus (in plane strain) and shear modulus, respectively. k_s is the shear correction factor, which is assumed equal to 5/6 in this investigation. In addition, we define the compliances, $a_k = 1/A_k$, $c_k = 1/C_k$, and $d_k = 1/D_k$.

2.2. Adhesive model

For each segment S_i, according to Timoshenko's beam theory the displacements u_i and w_i, respectively along axial and transverse directions, are approximated by:

$$\begin{cases} u_i = u_i\left(x_j, z_i\right) = u_i^{\mathrm{o}}\left(x_j\right) + z_i \phi_i\left(x_j\right), \\ w_i = w_i\left(x_j\right). \end{cases} \tag{1}$$

Because the thickness h_a of the adhesive is much smaller than the thicknesses of both the chip and substrate layers, we can neglect any variation of the stresses and strains in the adhesive layer along the z-direction. In particular, the strain components at a point in the adhesive are approximated by their mean values computed from the relative displacements at the top and bottom surfaces of the adherend layers (da Silva et al., 2009). Hence:

$$\begin{cases} \varepsilon_{zz}^a = \dfrac{w_2^{\mathrm{top}} - w_1^{\mathrm{bottom}}}{h_a} = \dfrac{w_2\left(-h_2\right) - w_1\left(h_1\right)}{h_a} = \dfrac{w_2 - w_1}{h_a}, \\ \gamma_{xz}^a = \dfrac{u_2^{\mathrm{top}} - u_1^{\mathrm{bottom}}}{h_a} = \dfrac{u_2\left(-h_2\right) - u_1\left(h_1\right)}{h_a} = \dfrac{u_2^{\mathrm{o}} - u_1^{\mathrm{o}} - h_1\phi_1 - h_2\phi_2}{h_a}, \end{cases} \tag{2}$$

where h_1(= H_1/2) and h_2(= H_2/2) are the half thicknesses of the chip and substrate, respectively. It needs to be noted that the term, $\left[\mathrm{d}w_1/\mathrm{d}x_1 + \mathrm{d}w_2/\mathrm{d}x_1\right]/2$ that has negligible effects reported in Chadegani et al. (2011), is simplified. Under the assumption of plane strain conditions, the relationship between the adhesive normal strains in the x- and z-directions is $\varepsilon_{xx}^a = -\nu_a/(1-\nu_a)\varepsilon_{zz}^a$ (Yang et al., 2008). If assume that the adhesive longitudinal normal stress is negligible, only shear

stress and transverse normal stress (the peel stress) exist in the adhesive. By Hooke's Law the peel stress and adhesive shear stress can be determined by:

$$\begin{cases} \sigma = \dfrac{E_a}{(1+\nu_a)(1-2\nu_a)}\left[\nu_a \varepsilon_{xx}^a + (1+\nu_a)\varepsilon_{zz}^a\right] = \dfrac{E_a}{1-\nu_a^2}\varepsilon_{zz}^a, \\ \tau = G_a \gamma_{xz}^a. \end{cases} \tag{3}$$

Based on the aforementioned assumptions, the adhesive layer is considered as a zero-thickness elastic interface, which consists of a uniform, continuous distribution of springs acting in the normal and tangential directions with respect to the interface plane. Accordingly, we define the peel stiffness, k_σ, and shear stiffness, k_τ. A simple, yet effective estimate of the latter constants is given by $k_\sigma = E_a^* / h_a$ and $k_\tau = G_a / h_a$, where $E_a^* = E_a / (1 - \nu_a^2)$ and $G_a = E_a / [2(1 + \nu_a)]$ respectively are the Young's modulus (in plane strain) and shear modulus of the adhesive. Therefore:

$$\begin{cases} \sigma = k_\sigma (w_2 - w_1), \\ \tau = k_\tau \left(u_2^{\circ} - u_1^{\circ} - h_1\phi_1 - h_2\phi_2\right). \end{cases} \tag{4}$$

2.3. Equilibrium equations

2.3.1. Region 1

Fig.2 shows free-body diagrams of elementary segments of the chip and substrate layers in Region 1 ($x_1 \in [0, l_1]$), describing the forces and moments as well as the adhesive shear and peel stresses. Considering the three equilibrium requirements for each adherend, the following differential equations hold:

$$\begin{cases} \dfrac{\mathrm{d}N_1}{\mathrm{d}x_1} + \tau = 0, \quad \dfrac{\mathrm{d}Q_1}{\mathrm{d}x_1} + \sigma = 0, \quad \dfrac{\mathrm{d}M_1}{\mathrm{d}x_1} + h_1\tau - Q_1 = 0; \\ \dfrac{\mathrm{d}N_2}{\mathrm{d}x_1} - \tau = 0, \quad \dfrac{\mathrm{d}Q_2}{\mathrm{d}x_1} - \sigma = 0, \quad \dfrac{\mathrm{d}M_2}{\mathrm{d}x_1} + h_2\tau - Q_2 = 0; \end{cases} \tag{5}$$

where the internal forces are given by the constitutive laws of a Timoshenko beam:

$$N_i = A_k \frac{\mathrm{d}u_i^{\circ}}{\mathrm{d}x_j}, \quad Q_i = C_k\left(\frac{\mathrm{d}w_i}{\mathrm{d}x_j} + \phi_i\right), \quad M_i = D_k \frac{\mathrm{d}\phi_i}{\mathrm{d}x_j}. \tag{6}$$

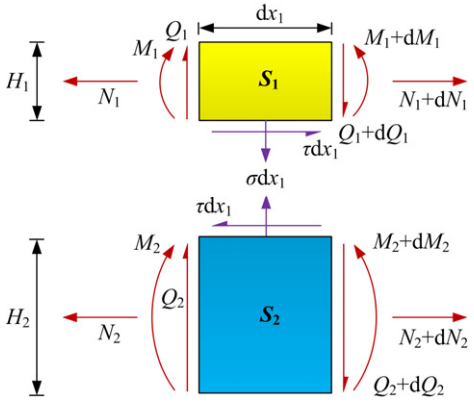

Fig.2. Free-body diagrams of elementary segments of the chip and substrate in Region 1.

By substituting Eq.(6) into Eq.(5), one can derive the following governing differential equations, which establish a relationship between the adherends' displacements and the adhesive stresses:

$$\begin{cases} \dfrac{\mathrm{d}^2 u_1^{\mathrm{o}}}{\mathrm{d}x_1^2} = -a_1\tau; \quad \dfrac{\mathrm{d}\phi_1}{\mathrm{d}x_1} + \dfrac{\mathrm{d}^2 w_1}{\mathrm{d}x_1^2} = -c_1\sigma; \quad \dfrac{\mathrm{d}^3\phi_1}{\mathrm{d}x_1^3} = -d_1\sigma - d_1 h_1 \dfrac{\mathrm{d}\tau}{\mathrm{d}x_1}; \\ \dfrac{\mathrm{d}^2 u_2^{\mathrm{o}}}{\mathrm{d}x_1^2} = a_2\tau; \quad \dfrac{\mathrm{d}\phi_2}{\mathrm{d}x_1} + \dfrac{\mathrm{d}^2 w_2}{\mathrm{d}x_1^2} = c_2\sigma; \quad \dfrac{\mathrm{d}^3\phi_2}{\mathrm{d}x_1^3} = d_2\sigma - d_2 h_2 \dfrac{\mathrm{d}\tau}{\mathrm{d}x_1}. \end{cases} \tag{7}$$

2.3.2. Region 2

Fig.3 shows the free-body diagram of an elementary segment of the substrate layer in Region 2 ($x_{2\in}$ [0, l_2]). The following equilibrium equations can be deduced:

$$\frac{\mathrm{d}N_3}{\mathrm{d}x_2} = 0, \quad \frac{\mathrm{d}Q_3}{\mathrm{d}x_2} = 0, \quad \frac{\mathrm{d}M_3}{\mathrm{d}x_2} - Q_3 = 0. \tag{8}$$

By substituting Eq.(6) into Eq.(8), one obtains:

$$\frac{\mathrm{d}^2 u_3^{\mathrm{o}}}{\mathrm{d}x_2^2} = 0, \quad \frac{\mathrm{d}\phi_3}{\mathrm{d}x_2} + \frac{\mathrm{d}^2 w_3}{\mathrm{d}x_2^2} = 0, \quad \frac{\mathrm{d}^3\phi_3}{\mathrm{d}x_2^3} = 0. \tag{9}$$

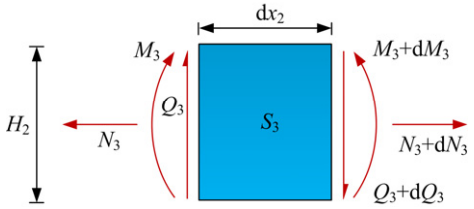

Fig.3. Free-body diagram of an elementary segment of the substrate in Region 2.

2.4. Boundary and continuity conditions

Recalling the scheme of Fig.1(c), the boundary and continuity conditions for the problem at hand can be defined as follows:

a) symmetry conditions at the left-hand end section of Region 1:

$$\begin{aligned} u_1^{\circ}\big|_{x_1=0} = 0, \quad \phi_1\big|_{x_1=0} = 0, \quad Q_1\big|_{x_1=0} = 0; \\ u_2^{\circ}\big|_{x_1=0} = 0, \quad \phi_2\big|_{x_1=0} = 0, \quad Q_2\big|_{x_1=0} = 0; \end{aligned} \tag{10}$$

b) free end conditions at the right-hand end section of the chip layer in Region 1:

$$N_1\big|_{x_1=l_1} = 0, \quad Q_1\big|_{x_1=l_1} = 0, \quad M_1\big|_{x_1=l_1} = 0; \tag{11}$$

c) continuity conditions at the cross sections connecting segments S_2 and S_3 of the substrate layer:

$$\begin{aligned} u_2^{\circ}\big|_{x_1=l_1} = u_3^{\circ}\big|_{x_2=0}, \quad \phi_2\big|_{x_1=l_1} = \phi_3\big|_{x_2=0}, \quad w_2\big|_{x_1=l_1} = w_3\big|_{x_2=0}; \\ N_2\big|_{x_1=l_1} = N_3\big|_{x_2=0}, \quad Q_2\big|_{x_1=l_1} = Q_3\big|_{x_2=0}, \quad M_2\big|_{x_1=l_1} = M_3\big|_{x_2=0}; \end{aligned} \tag{12}$$

d) periodicity conditions at the right-hand end section of the substrate layer in Region 2:

$$N_3\big|_{x_2=l_2} = PH_2, \quad \phi_3\big|_{x_2=l_2} = 0, \quad w_3\big|_{x_2=l_2} = 0. \tag{13}$$

3. Adhesive stresses

3.1. Analytical model

3.1.1. Adhesive stresses

As described by da Silva et al. (2009), it is not straightforward to obtain a closed-form solution of the differential problem formulated by Eqs.(5) or (7) in the general case. As the model or boundary conditions get more general, the governing equations become increasingly complicated and a computer has to be used for the solution. Generally speaking, there are two classes of computer-based solution methods. One strategy is to directly solve the differential equations numerically (Yang et al., 1996, 2008 and Chadegani et al., 2011, 2012). Another one is to calculate numerically the values of select constants parameters (roots of the characteristic equation, integration constants *etc.*), given an analytical solution of the differential problem. The latter one is adopted here to calculate the distribution of the adhesive shear and peel stresses in the bonding region. To this aim, the adhesive stresses are assumed as the main unknowns, so that Eq.(7) is reduced to two uncoupled sixth and seventh order differential equations for the adhesive peel and shear stresses, respectively. Here, we limit our attention on describing how to determine the values of the integration constants for the present problem, by suitably applying the aforementioned boundary and continuity conditions. Other details of the solution strategy can be found in the Appendix.

By combining Eqs.(4) and (7) the following sixth order differential equation for the adhesive

peel stress is obtained:

$$\frac{\mathrm{d}^6\sigma}{\mathrm{d}x_1^6}+\eta_1\frac{\mathrm{d}^4\sigma}{\mathrm{d}x_1^4}+\eta_2\frac{\mathrm{d}^2\sigma}{\mathrm{d}x_1^2}+\eta_3\sigma=0 \tag{14}$$

where $\eta_1=-k_\tau\left(a_1+a_2+d_1h_1^2+d_2h_2^2\right)-k_\sigma\left(c_1+c_2\right)$, $\eta_2=k_\tau k_\sigma\left(a_1+a_2+d_1h_1^2+d_2h_2^2\right)\left(c_1+c_2\right)+k_\sigma\left(d_1+d_2\right)$ and $\eta_3=-k_\tau k_\sigma\left[\left(a_1+a_2\right)\left(d_1+d_2\right)+d_1d_2\left(h_1+h_2\right)^2\right]$. The characteristic equation for the peel stress is:

$$\lambda^6+\eta_1\lambda^4+\eta_2\lambda^2+\eta_3=0 \tag{15}$$

If $\Lambda=\lambda^2$, Eq.(15) is transformed into a cubic equation for Λ, whose root properties depend on $\Delta\left(=q^2/4+p^3/27\right)$, where $p=\eta_2+\eta_1^2/3$ and $q=2\eta_1^3/27-\eta_1\eta_2/3+\eta_3$. When the adhesive is relatively thick, $\Delta>0$ and the cubic equation has one real root and one pair of conjugate complex roots. However, when the adhesive layer is very thin, $\Delta<0$ and there are three real roots (Luo and Tong, 2009). Similarly, the adhesive shear stress is described by a seventh order differential equation:

$$\frac{\mathrm{d}^7\tau}{\mathrm{d}x_1^7}+\eta_1\frac{\mathrm{d}^5\tau}{\mathrm{d}x_1^5}+\eta_2\frac{\mathrm{d}^3\tau}{\mathrm{d}x_1^3}+\eta_3\frac{\mathrm{d}\tau}{\mathrm{d}x_1}=0 \tag{16}$$

It is obvious that Eqs.(14) and (16) show a resounding similarity. In fact, in addition to a zero root the shear stress equation has the same six roots of the peel stress equation. Therefore, we write the general expressions for the peel and shear stresses as:

$$\begin{cases}\sigma\left(x_1\right)=\sum_{n=1}^{6}F_n\exp\left(\lambda_nx_1\right),\\ \tau\left(x_1\right)=-\dfrac{1}{d_1h_1-d_2h_2}\left\{\sum_{n=1}^{6}F_n\left[\dfrac{\lambda_n^3}{k_\sigma}-\left(c_1+c_2\right)\lambda_n+\dfrac{d_1+d_2}{\lambda_n}\right]\exp\left(\lambda_nx_1\right)+F_7\right\},\end{cases} \tag{17}$$

where F_1, F_2, …, F_7 are integration constants, which are determined by the boundary and continuity conditions.

3.1.2. Integration constants

For Region 1, the internal forces can be obtained by substituting Eq.(17) into (5), and integrating the latter with respect to x_1. In turn, the expressions for the internal forces are substituted into Eq.(6). Then, integrating with respect to x_1, the expressions for the displacements are also derived. In this process, twelve new integration constants, F_8, F_9, …, F_{19}, appear (See Eqs.(A.1) - (A.6) in the Appendix for details).

For Region 2, Eq.(9) is solved to yield directly the expressions for the displacements of the substrate. The expressions for the internal forces are then deduced by substituting the displacements into Eq.(6) and taking the derivative with respect to x_2, as shown in Eqs.(A.7) and (A.8). The

obtained expressions involve seven more integration constants, F_{20}, F_{21}, …, F_{26}.

To sum up, there are 26 total integration constants to be determined. However, not all of them are concerned, except for the first seven constants entering the expressions for σ and τ. Furthermore, these constants are not all independent of each other. In fact, we observe that when the expressions for the adhesive stresses and displacements in Region 1 are introduced into Eq.(4), seven relationships among the constants emerge, as shown in Eq.(A.9). For Region 2, an additional relationship is deduced by substituting the expressions for Q_3 and M_3 into Eq.(6), as shown in Eq.(A.10). Hence, all the 26 integration constants can be determined by using the 8 relationships among the integration constants and the 18 boundary and continuity conditions Eqs.(10) - (13). Via mathematical operation (executed by Maple software), we find that eight integration constants, namely F_7, F_9, F_{12}, F_{14}, F_{15}, F_{17}, F_{18}, and F_{22}, are zero, while the first six constants, namely, F_1, F_2, …, F_6, are given by the solution of the following linear equation set:

$$\begin{aligned}
&\sum_{n=1}^{6} F_n \frac{1}{\lambda_n} = 0, \\
&\sum_{n=1}^{6} F_n \frac{1}{\lambda_n^3} = 0, \\
&\sum_{n=1}^{6} F_n \lambda_n = 0, \\
&\sum_{n=1}^{6} F_n \frac{\exp(\lambda_n l_1)}{\lambda_n} = 0, \\
&\sum_{n=1}^{6} F_n \left\{ \alpha_1 \left[\frac{\lambda_n^2}{k_\sigma} - (c_1 + c_2) \right] + \frac{\lambda_n}{k_\sigma} + \alpha_2 \left(\frac{1}{\lambda_n^3} - \frac{l_1}{\lambda_n^2} \right) \right\} \exp(\lambda_n l_1) = 0, \\
&\sum_{n=1}^{6} F_n \left\{ \beta_1 \left[\frac{\lambda_n^2}{k_\sigma} - (c_1 + c_2) \right] + \frac{\beta_2}{\lambda_n^2} \right\} \exp(\lambda_n l_1) = 2a_2 h_2 (d_2 h_2 - d_1 h_1) P,
\end{aligned} \tag{18}$$

where $\alpha_1 = l_2 - d_1h_1(l_1 + l_2) / d_2h_2$, $\alpha_2 = d_1(h_1 + h_2) / h_2$, $\beta_1 = (a_1 + a_2) + d_1h_1(h_1 + h_2)$ and $\beta_2 = d_1d_2(h_1 + h_2)^2 + (a_1 + a_2)(d_1 + d_2)$. The process of solving the above linear equation set is performed using the MATLAB (R2010b) software. Then, the analytical expressions of the adhesive stresses are obtained by substituting the first seven integration constants into Eq.(17).

3.2. Numerical example

As an illustrative example, we consider the chip-on-substrate structure characterized by the geometrical dimensions and material properties listed in Table 1 from Ref. Saiki et al. (2010). The substrate layer is subjected to a uniform tensile stress P = 5MPa on the right-hand end section of Region 2.

Table 1 Geometrical dimensions and material properties for the illustrative example.

Layers	Thickness (μm)	Young's modulus (MPa)	Poisson's ratio	Material
Chip	100	129,000	0.28	Silicon
Adhesive	5	20	0.40	Acryl/epoxy resins
Substrate	100	160	0.45	Polyolefin

In order to check the analytical results, a finite element model of the chip-on-substrate structure has been defined and analyzed using the commercial code ABAQUS 6.10. In the computational model (Fig.4) all of the three layers (chip, adhesive and substrate) are assumed to be made of linearly elastic and isotropic materials. The whole structure is considered to deform under plane strain conditions, and a plane strain element, CPE4, is employed. The mesh sensitivity analysis has been performed by sequential refinement of the finite element mesh, shown in the Fig.5. Considering both convergence and computational cost, the mesh size is finally selected as 1×1μm in the adherends and 1×5/6μm in the adhesive. To impose the periodicity conditions, a reference point (RP) is defined and coupled with the right-hand vertical surface in Region 2. The concentrated force applied to the reference point, $P_{\text{concentrated}}$ = 0.5N, is taken to correspond with the uniform tensile stress, P, applied in the analytical model. At the same time, the vertical and rotational degrees of freedom of the reference point are restricted. Other boundary conditions impose symmetry about the z-axis.

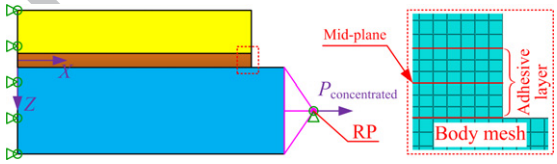

Fig.4. Scheme of the finite element model with boundary conditions and local mesh of the adhesive layer

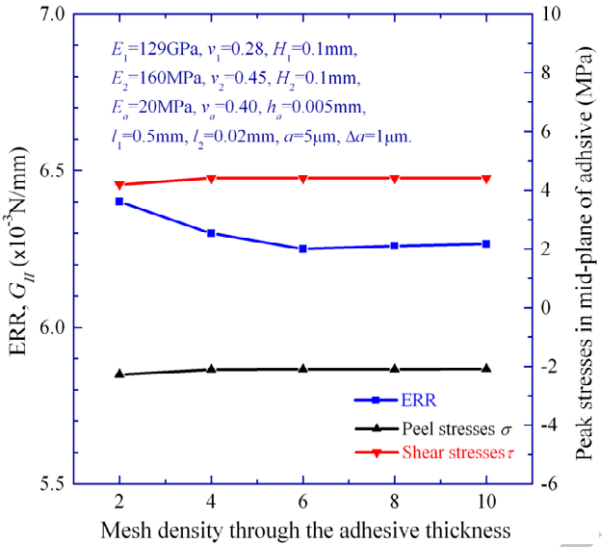

Fig.5. Convergence of adhesive stresses and ERR, G_{II}, versus mesh density through the adhesive thickness.

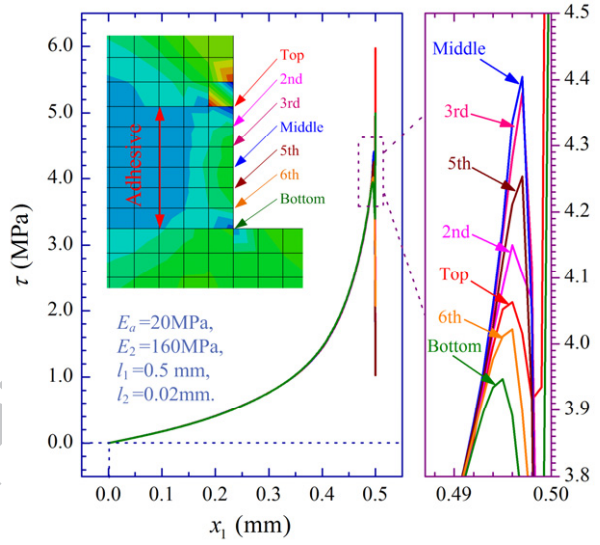

Fig.6. Shear stress in the adhesive layer versus the x_1-coordinate, at different levels included between the top and bottom interfaces, estimated by the FE model.

Fig.6 shows the distribution of the shear stress in the adhesive versus the x_1-coordinate, ranging from zero to l_1, as estimated by the finite element method, for l_1 = 0.5mm and l_2 = 0.02mm. The figure shows seven curves, each of which corresponds to a different value of the z-coordinate, ranging from the bottom to the top of the adhesive layer. All the plotted curves appear very close, except for the maximum values in the proximity of the joint right-hand edge. This result shows

indirectly that the variation of the stresses in the adhesive layer along the z-direction is very small when the adhesive is much thinner than the adherends. Furthermore, we observe that the maximum values of the shear stress at the mid-plane level are higher than those evaluated at the other levels except the singular stresses at the ends of both top and bottom adhesive interfaces (Gleich et al., 2001). Therefore, in the following we will always evaluate the stresses at the mid-plane.

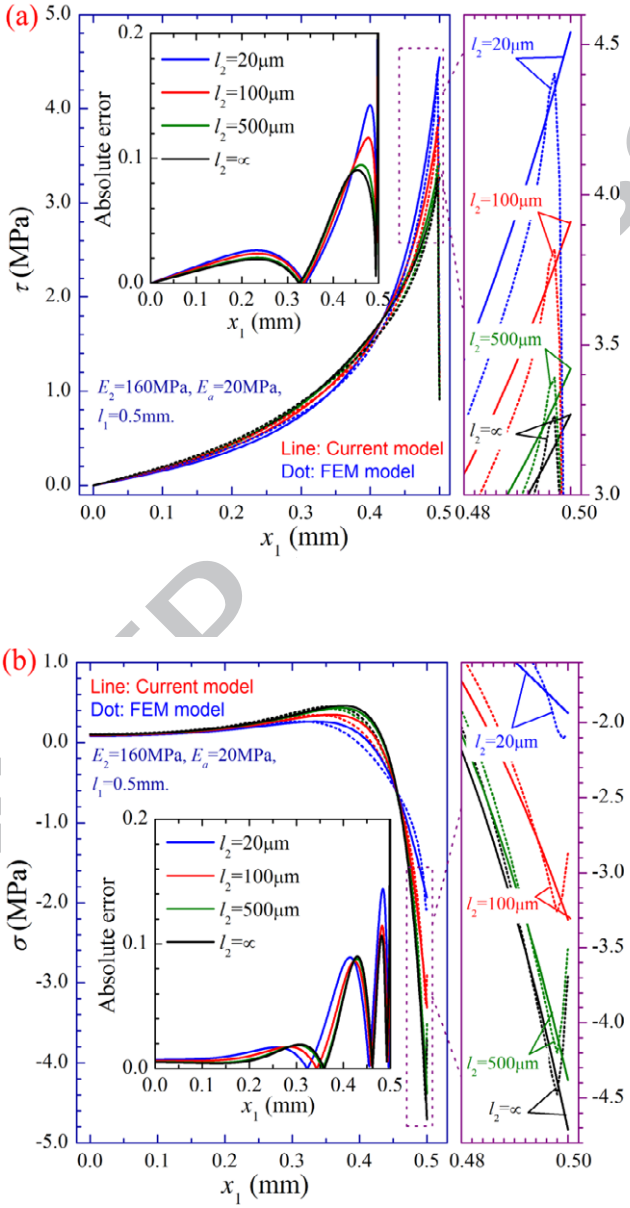

Fig.7. (a) and (b) are adhesive shear and peel stresses estimated by both the analytical model and the FE model with their absolute errors, respectively, versus the x_1-coordinate.

Fig.7 illustrates the distributions of the shear stress, τ, and peel stress, σ, in the adhesive layer, respectively, as estimated by the analytical model and the FEM. Several values (20, 100, 500μm, and ∞) of l_2 are considered in order to show the effects of the distance between the chips, while the length of chip is fixed at $2l_1$ = 1.0mm. Here, ∞ represents the traction-free boundary condition, namely the case of a single isolated chip on an infinite substrate, or the case of many chips that are spaced far away from each other such that their interactions can be neglected.

The analytical predictions and finite element results agree well except in the vicinity of the right-hand end of the curves, even better with regard to their trends. The absolute errors, i.e., $\left|\tau_{\text{Current model}}\left(x_1\right)-\tau_{\text{FEM}}\left(x_1\right)\right|$ and $\left|\sigma_{\text{Current model}}\left(x_1\right)-\sigma_{\text{FEM}}\left(x_1\right)\right|$, versus x_1 are shown simultaneously, indicating the peak stresses can be estimated well whose relative errors of both the shear and peel stresses are 2.9%, 1.8%, 0.8%, 0.5% and 8.6%, 2.3%, 3.5%, 4.6% for l2 = 20, 100, 500 and ∞ μm, respectively. These differences in the vicinity of the right-hand occur because in the FE model the adhesive behaves as an elastic material and the shear stress at the free edge must be null because of the boundary conditions (this condition is not even fulfilled exactly because in the FEA the stresses are evaluated at internal integration points). Instead, according to the analytical solution, the adhesive stresses attain peak values at the free edge. In any case, it is worth mentioning that in a real joint, the adhesive would undergo plastic deformations and the stresses at the joint ends would be reduced.

From Fig.7(a), it can be seen that the shear stress decays very rapidly when moving away from the edge at $x_1 = l_1$. As the half distance, l_2, between the chips decreases (namely, as the chips are arrayed closer and therefore have stronger interaction), the adhesive shear stress, τ, increases rather quickly. The opposite effect is observed from Fig.7(b) for the peel stress, σ, which decreases quickly as the distance gets smaller. The value of σ for $l_2 = \infty$ is more than double that for l_2 = 20μm. We also observe that the peel stress has a self-equilibrated distribution, since the total force resulting from the peel stress must vanish. Besides, the peel stress has negative values near to the right-hand end section of the adhesive. This means that the adhesive layer is subjected to compression at the edge, when the chip layer is much stiffer than the substrate layer. Therefore, despite the presence of peel stresses, crack propagation is expected to occur under pure mode II conditions. Thus, only the mode II contribution to the ERR is relevant for the problem at hand and will be calculated in the following.

Based on the discussions above, we may conclude that the adhesive stresses computed according to the analytical model, albeit built on some simplifying assumptions, provide quite accurate estimates for the shear and peel stresses in the mid-plane of the adhesive, in particular for their maximum values. The method has accounted for the interactions among chips, and is rather accurate when the thickness of the adhesive layer is much smaller than those of the adherends.

4. Cohesive failure analysis

4.1. Analytical model and computation of energy release rate

In line with the analytical model, the model II contribution to the energy release rate can be computed as (Krenk, 1992; Shahin and Taheri, 2008):

$$G_{II} = \frac{\tau_{\text{Crack-tip}}^2}{2k_\tau}, \tag{19}$$

where $\tau_{\text{Crack-tip}}$ is the value of the shear stress at the crack tip, computed at the end of the elastic interface. It is worth noting that Eq.(19) furnishes finite values of G_{II} also when no initial crack is present.

In the finite element model, however, the virtual crack closure technique will be applied to estimate the ERR at the mid-plane of the adhesive layer affected by an existing crack. Preliminary computations have shown that Eq.(19) slightly overestimates the ERR with respect to the numerical model. This behavior can be related to the use of a finite, albeit very small, increment Δa for computing G_{II} in the numerical model, while Eq.(19) strictly holds in the limit $\Delta a \to 0$. Based on these considerations, in order to compare the analytical and numerical results for the ERR, it is convenient to apply an adaptation of the VCCT also for the analytical model instead of using Eq.(19).

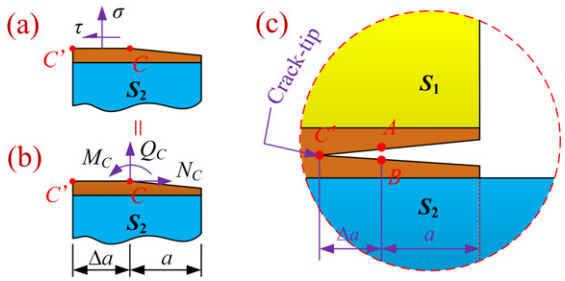

Fig.8. (a) Peel and shear stresses on the bottom crack surface, (b) equivalent concentrated forces

and couple at the crack tip, and (c) adhesive layer with an initial crack of length a and a virtual crack extension length Δa.

In this regard, we assume that an existing crack of length a, located at the mid-plane of the adhesive, extends by a small length Δa from point C to point C', see Fig.1(c). Before this virtual crack growth, non-zero shear and peel stresses in general exist at points located on the segment $C'C$ in the adhesive layer, as shown in Fig.8(a). Such stresses are statically equivalent to two concentrated forces acting in the axial and transverse directions, N_C and Q_C, and a couple, M_C, applied at the crack-tip, see Fig.8(b). When the virtual crack propagates from point C' to point C, the previous crack-tip C is assumed to split into two points A and B, see Fig.8(c). In order to close the small virtual crack increment, the crack-tip forces and couple have to be applied at points A and B to move them back to their original locations. The ERR due to a small increase in crack length is equivalent to the work required to close that small crack increment. The mode II contribution to the ERR can be written as (Yang et al., 2008):

$$G_{II} = \frac{1}{2\Delta a}\left[N_C\left(u_A - u_B\right)\right], \tag{20}$$

where N_C is the force equivalent to the shear stress exchanged between points C' and C, and ($u_A - u_B$) is the relative longitudinal displacement of points A and B. The latter quantities can be calculated as $N_C = -\int_{l_1-a-\Delta a}^{l_1-a} \tau(x_1)\mathrm{d}x_1$ and $[u_1(h_1) - u_2(-h_2)]$, respectively. Given Eqs.(1) and (4), the mode II ERR is finally written as:

$$G_{II} = \frac{\tau_C}{2\Delta a k_\tau}\int_{l_1-a-\Delta a}^{l_1-a} \tau(x_1)\mathrm{d}x_1, \tag{21}$$

where τ_C is the value of shear stress at point C. The mode II ERR is computed by substituting the expression of shear stress, the second term of Eq.(17), into Eq.(21).

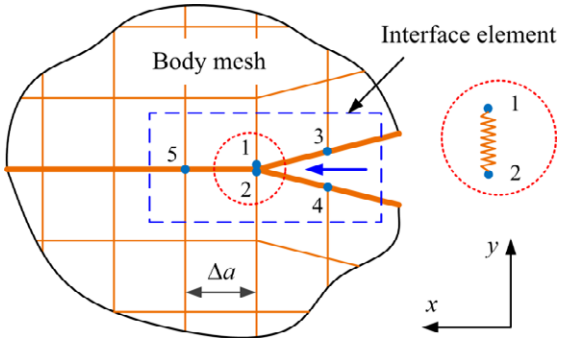

Fig.9. Fracture interface element with dummy nodes.

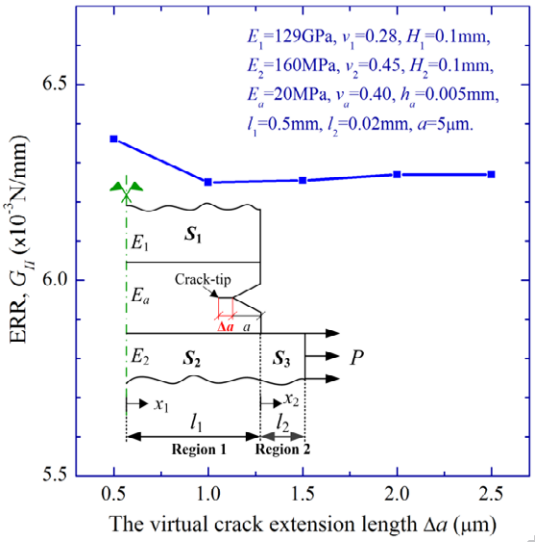

Fig.10. Convergence of ERR, G_{II}, as a function of the virtual crack extension length, Δa.

In order to ascertain the accuracy of Eq.(21), we compare its predictions with the results obtained by using the VCCT with dummy nodes. To this aim, we have used the fracture interface element, shown in the Fig.9, implemented by user-defined element subroutines (UEL) in ABAQUS 6.10. These special elements enable the calculation of the ERR in conjunction with the FEA. Concerning the details of the VCCT with dummy nodes, we refer the reader to the original papers by Xie and Biggers (2006, 2007) and Peng et al. (2011, 2012). It is worth emphasizing that, when using the VCCT, we assume the crack path is embedded in the middle of the adhesive layer, as shown in Fig.1(c). In view of the effect of the virtual extension length Δa on ERR (Chadegani et al., 2012), as shown in Fig.10, we consider an initial crack length a = 5μm and a propagation length Δa = 1μm in order to calculate ERR using the VCCT with dummy nodes. All the other variables have the same values shown in Table 1.

4.2. Effects of geometrical dimensions

The key parameters of the periodic array of chips are the distance between the chips and the length of the chips. Therefore, in the following we will focus on the effects of these two geometrical dimensions on the debonding behavior.

4.2.1. Effects of the distance between the chips

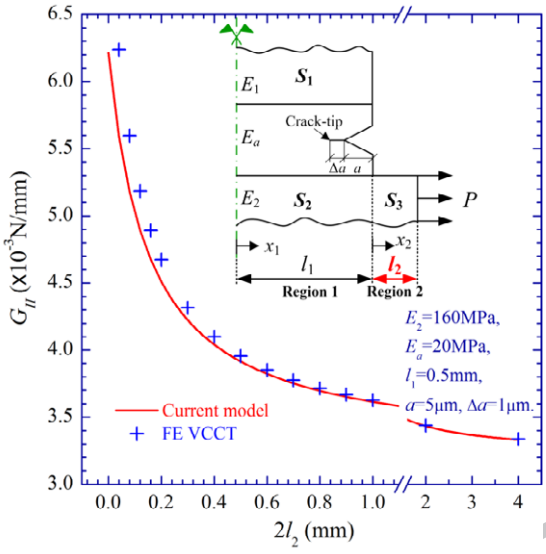

Fig.11. Mode II energy release rate as a function of the distance between the chips.

Fig.11 depicts the energy release rate, G_{II}, for a crack embedded in the midline of the adhesive versus the distance between the chips, $2l_2$. The continuous curve refers to the analytical model and has been obtained by using Eq.(21). Points represented by crosses have been obtained from the FE model by using the VCCT with dummy nodes. The length of the chip is fixed at $2l_1$ = 1.0mm. The distance between the chips, $2l_2$, varies from 0.04mm to 4.0mm. Analytical and numerical results match fairly well in the entire range of variation of $2l_2$. The ERR decreases as the distance between the chips becomes larger. Greater variations in the ERR are observed for a distance between the chips smaller than 0.6mm, which indicates that interaction is stronger when the chips are arrayed closer to each other. Instead, if the interval between neighboring chips is quite large, the strain resulting from tensioning the substrate is mainly accommodated by the portion of substrate between the chips. In this cases, the strain in the chips is negligible and its influence on the ERR is small. In conclusion, we may say that the density of the chips has large effects on the ERR of the chip-on-substrate structure.

4.2.2. Effects of the chip size

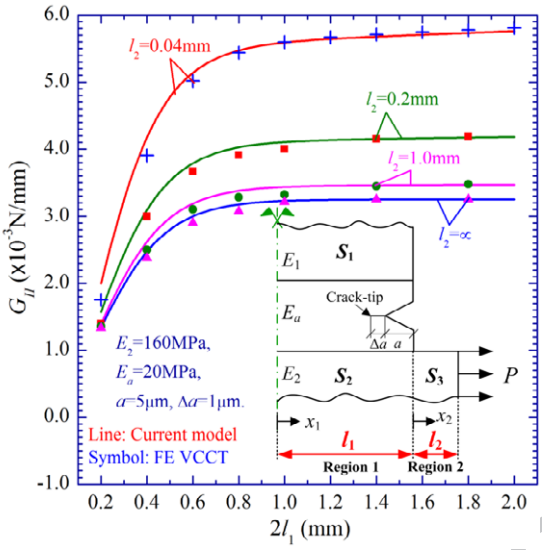

Fig.12. Mode II energy release rate as a function of the chip size.

Fig.12 plots the mode II contribution to the ERR, G_{II}, versus the chip size, $2l_1$. Several values (0.04, 0.2, 1.0mm, and ∞) of l_2 are considered in order to show also the effects of the distance between the chips. The length of the chip varies from 0.2mm to 2.0mm, which covers both small and large chips used in industry. Analytical (continuous curves) and numerical (single points) results agree very well, except for some slight deviations observed for small values of $2l_1$. We observe that the ERR increases as the length of the chips increases, because the strain level in the adhesive becomes smaller as the chips reduce in size. However, the ERR becomes practically constant when the chip size is larger than 0.8mm. Concerning the effects of the distance between the chips, we note that smaller intervals correspond to higher values of the ERR. However, above a certain value of l_2, there is no practical variation in the ERR, which means that this effect becomes weaker when the chips are spaced far away from each other. In conclusion, we may say that the length of the chips has a strong effect on the ERR when the chip size is small, and almost no effect when the chip size is large (in this case, more than 0.8mm). Additionally, the distance between the chips aggravates the effects of the chip size on the ERR.

4.3. Effects of material properties

4.3.1. Effects of the elastic modulus of the substrate

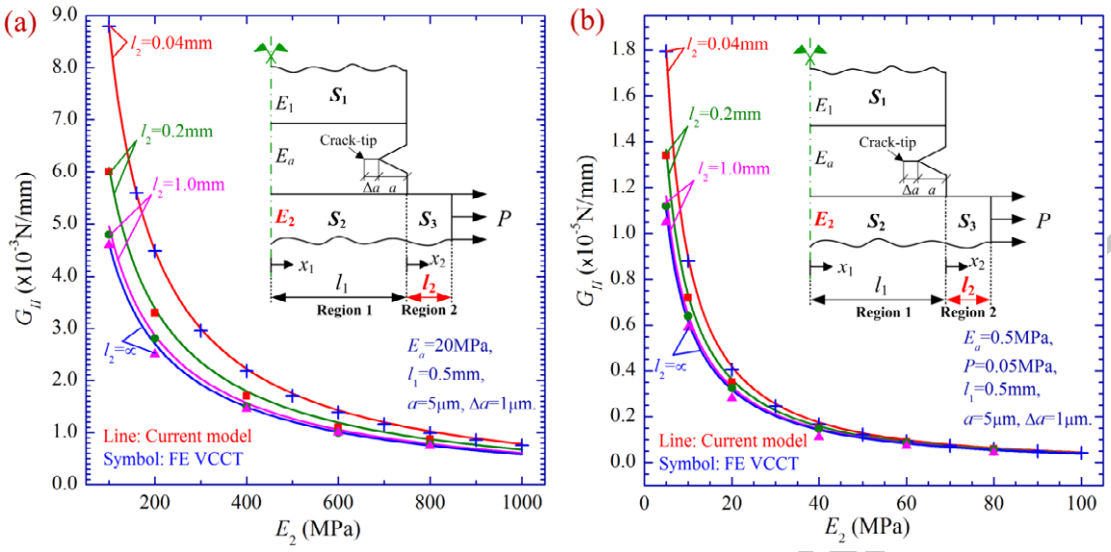

Fig.13. Mode II energy release rate as a function of the elastic modulus of the substrate: (a) general adhesive and substrates; (b) very compliant adhesive and substrates.

Fig.13 depicts the mode II contribution to the ERR, G_{II}, versus the elastic modulus of the substrate, E_2, for several values of the half distance between adjacent chips, l_2. The chip size is fixed at $2l_1$ = 1.0mm, other parameters have the values given in Table 1. In particular, Fig.13(a) refers to a general adhesive (E_a = 20MPa) and substrates (E_2 ranging from 100MPa to 1000MPa). Instead, Fig.13(b) refers to a very compliant adhesive (E_a = 0.5MPa) and substrates (E_2 ranging from 5MPa to 100MPa): this case corresponds, for instance, to rubber substrates used in stretchable electronics. The figure shows how the values obtained from the finite element model using the VCCT (single points) and the analytical model (continuous curves) are almost identical. We note that ERR increases as the substrate becomes more compliant. This means that chips-on-substrate structures having very compliant substrates are more exposed to the premature debonding of the IC chips. This trend is understood as follows: if the substrate is more compliant, the adhesive gets more strained to accommodate the deformation of the substrate layer, so that the generation in strain energy is greater. Based on the above results, we may conclude that the mechanical properties of the substrate have very important effects on the ERR. Additionally, we note that the analytical model presented in this paper can accurately predict the debonding of the IC chips from different substrates, ranging from rubber to polymer.

4.3.2. Effects of the elastic modulus of the adhesive

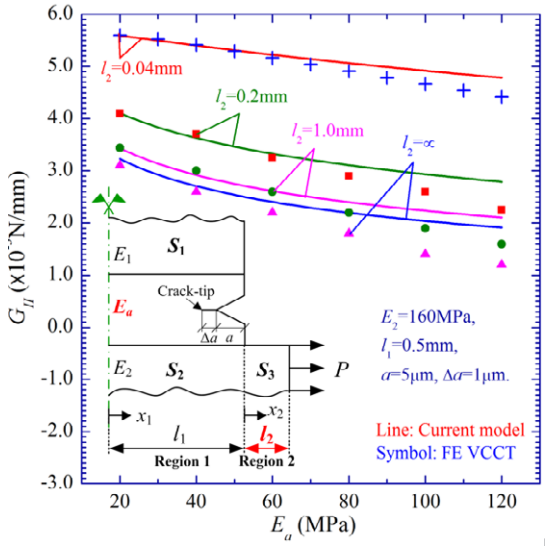

Fig.14. Mode II energy release rate as a function of the elastic modulus of adhesive.

Fig.14 plots the mode II ERR, G_{II}, as a function of the elastic modulus of the adhesive, E_a. The chip size is fixed at $2l_1$ = 1.0mm. In practical applications, the adhesive layer needs to be more compliant than the substrate. Therefore, the elastic modulus of the adhesive is varied here from 20MPa to 120MPa. The analytical (continuous curves) and numerical (single points) results agree very well. Both methods predict monotonic decreasing trends for the ERR with the elastic modulus of the adhesive. However, this dependency appears quite weak, suggesting that the ERR is almost insensitive to it in practice. This behavior can be explained qualitatively by recalling Eqs.(20) and (21). Although the relative axial displacement increases as the adhesive becomes more compliant, the axial force decreases, which results in small variations of the ERR. Slight deviations of the analytical predictions from the numerical results are observed with the increase of E_a. Finally, by observing the curves plotted for different values of l_2, we note that the effects of the variation of the adhesive stiffness are, in percentage, more significant when the chips are spaced far away from each other (da Silva et al., 2009).

4.4. Design considerations

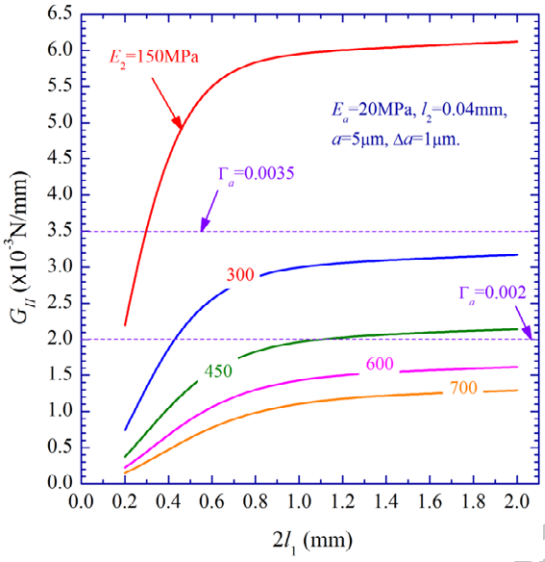

Fig.15. Maximum energy release rate as a function of the chip size.

In practice, for a given chip-on-substrate structure, the geometrical dimensions and material properties are fixed values, depending on service and manufacturing issues. The only design parameter which can be easily changed is the value of the applied tension. The above results can help optimization of the technological process by calculating in advance the most suitable value of the tensile force. Here, we illustrate how to apply the results obtained in the previous sections to prevent premature debonding of the chips from the substrate. Fig.15 plots the mode II ERR, G_{II}, as a function of the chip size, $2l_1$, for several values of E_2, ranging from 150MPa to 750MPa. The interval between adjacent chips is fixed at $2l_2$ = 0.08mm. If the fracture toughness of the adhesive, Γ_a, is known, this plot gives a way to determine the critical elastic modulus of the substrate layer or the critical chip size, corresponding to adhesive debonding under prescribed uniaxial tension. For example, assuming Γ_a = 0.002 N/mm, the critical chip size can almost triplicate if the substrate stiffness increases from 300MPa to 450MPa. If Γ_a = 0.0035 N/mm, the chips will never delaminate from the substrate in the entire range of variation of $2l_1$, under the same conditions, as long as the stiffness of the substrate is not less than 300MPa.

5. Conclusions

An analytical model has been presented to investigate the mechanical behavior of a layered structure consisting of a periodic array of IC chips bonded to a stretched substrate. The stresses and

ERR developing in the adhesive layer have been identified with those characterizing an equivalent elastic interface. Analytical expressions for the adhesive stresses and ERR have been given in terms of geometrical dimensions and material properties, while the values of the integration constants have been obtained numerically by using the multi-segment analysis method. Although it is necessary to use a computer implementation, this method is still advantageous if compared to other closed-form solutions because many of these also require some form of computing power. For comparison, a FEA has been carried out to compute the stresses in the adhesive layer and compare these with the analytical predictions for the adhesive stresses. Furthermore, the VCCT has been used to calculate the ERR. Excellent agreement has been found between the theoretical predictions of the model and the results of numerical analyses, considering the effects of key factors, including the distance between adjacent chips, chip size, adhesive and substrate material properties.

Both the analytical and numerical models show that the peel stresses at the crack tip are always negative (compressive) for the problem at hand. Therefore, crack propagation is expected to occur under pure mode II conditions. Thus, only the mode II contribution to the ERR has been considered in our study. Based on the presented analytical model, the effects of the geometrical dimensions and material properties of the chip-on-substrate structure have been investigated in detail. The interaction between the chips has shown a remarkable influence on the adhesive stresses, which becomes stronger, especially, for chips very closely arrayed on the substrate. Under the same load level, at high values of the ratio of the chip distance to the chip size, most of the deformation is accommodated by the substrate, while smaller strains affect the adhesive layer. Therefore, also the influence on the energy release rate becomes smaller. We have also shown that the probability of debonding of the IC chips from the substrate increases as the substrate and adhesive layers become more compliant. Finally, the ERR has turned out to be quite insensitive to the elastic properties of the adhesive in the practical range of variation (E_a / E_2 < 1). In the future, we will apply the proposed methodology to derive design rules for the pick-up process of advanced IC packages, which will be the subject of a forthcoming paper.

Acknowledgements

This work is supported by the National Natural Science Foundation of China (51035002, 51175209, 51121002) and New Century Excellent Talents in University (NCET-11-0171). The

authors gratefully acknowledge Dr. Bo Peng and MS Wei Li of HUST, China, for huge help in calculation.

Appendix A

A.1. Internal forces and displacements in Region 1

For Region 1, the internal force can be obtained by substituting the expressions of adhesive stresses Eq.(17) into Eq.(5), and integrating the letter with respect to x_1.

$$\begin{aligned} N_1(x_1) &= \frac{1}{d_1h_1 - d_2h_2}\left\{\begin{array}{l}\sum_{n=1}^{6} F_n\left[\frac{\lambda_n^2}{k_\sigma} - (c_1+c_2) + \frac{d_1+d_2}{\lambda_n^2}\right]\exp(\lambda_n x_1)\\ +F_7 x_1 + F_8\end{array}\right\},\\ N_2(x_1) &= -\frac{1}{d_1h_1 - d_2h_2}\left\{\begin{array}{l}\sum_{n=1}^{6} F_n\left[\frac{\lambda_n^2}{k_\sigma} - (c_1+c_2) + \frac{d_1+d_2}{\lambda_n^2}\right]\exp(\lambda_n x_1)\\ +F_7 x_1 + F_{11}\end{array}\right\}\end{aligned} \tag{A.1}$$

for the axial forces;

$$\begin{aligned} Q_1(x_1) &= -\left[\sum_{n=1}^{6} F_n \frac{1}{\lambda_n}\exp(\lambda_n x_1) + F_9\right],\\ Q_2(x_1) &= \sum_{n=1}^{6} F_n \frac{1}{\lambda_n}\exp(\lambda_n x_1) + F_{12}\end{aligned} \tag{A.2}$$

for the shear forces; and lastly,

$$\begin{aligned} M_1(x_1) &= \frac{h_1}{d_1h_1 - d_2h_2}\left\{\begin{array}{l}\sum_{n=1}^{6} F_n\left[\frac{\lambda_n^2}{k_\sigma} - (c_1+c_2) + \frac{d_2(h_1+h_2)}{h_1\lambda_n^2}\right]\exp(\lambda_n x_1)\\ +\left(F_7 - \frac{d_1h_1 - d_2h_2}{h_1}F_9\right)x_1 + F_{10}\end{array}\right\},\\ M_2(x_1) &= \frac{h_2}{d_1h_1 - d_2h_2}\left\{\begin{array}{l}\sum_{n=1}^{6} F_n\left[\frac{\lambda_n^2}{k_\sigma} - (c_1+c_2) + \frac{d_1(h_1+h_2)}{h_2\lambda_n^2}\right]\exp(\lambda_n x_1)\\ +\left(F_7 + \frac{d_1h_1 - d_2h_2}{h_2}F_{12}\right)x_1 + F_{13}\end{array}\right\}\end{aligned} \tag{A.3}$$

for the bending moments.

In turn, the expressions for internal forces, Eqs.(A.1) - (A.3), are substituted into Eq.(6). Then, integrating the letter with respect to x_1, the expressions for the displacements are also derived. The axial mid-plane displacements of segments S_1 and S_2 respectively are:

$$
\begin{aligned}
u_1^{\circ}(x_1) &= \frac{a_1}{d_1h_1 - d_2h_2}\left\{\begin{array}{l}\displaystyle\sum_{n=1}^{6} F_n\left(\frac{\lambda_n}{k_\sigma} - \frac{c_1+c_2}{\lambda_n} + \frac{d_1+d_2}{\lambda_n^3}\right)\exp(\lambda_n x_1) \\ \displaystyle +\frac{1}{2}F_7 x_1^{\,2} + F_8 x_1 + F_{14}\end{array}\right\}, \\
u_2^{\circ}(x_1) &= -\frac{a_2}{d_1h_1 - d_2h_2}\left\{\begin{array}{l}\displaystyle\sum_{n=1}^{6} F_n\left(\frac{\lambda_n}{k_\sigma} - \frac{c_1+c_2}{\lambda_n} + \frac{d_1+d_2}{\lambda_n^3}\right)\exp(\lambda_n x_1) \\ \displaystyle +\frac{1}{2}F_7 x_1^{\,2} + F_{11} x_1 + F_{17}\end{array}\right\}.
\end{aligned}
\tag{A.4}
$$

The rotations of the cross sections are:

$$
\begin{aligned}
\phi_1(x_1) &= \frac{d_1h_1}{d_1h_1 - d_2h_2}\left\{\begin{array}{l}\displaystyle\sum_{n=1}^{6} F_n\left[\frac{\lambda_n}{k_\sigma} - \frac{c_1+c_2}{\lambda_n} + \frac{d_2(h_1+h_2)}{h_1\lambda_n^3}\right]\exp(\lambda_n x_1) \\ \displaystyle +\frac{1}{2}\left(F_7 - \frac{d_1h_1 - d_2h_2}{h_1}F_9\right)x_1^{\,2} + F_{10}x_1 + F_{15}\end{array}\right\}, \\
\phi_2(x_1) &= \frac{d_2h_2}{d_1h_1 - d_2h_2}\left\{\begin{array}{l}\displaystyle\sum_{n=1}^{6} F_n\left[\frac{\lambda_n}{k_\sigma} - \frac{c_1+c_2}{\lambda_n} + \frac{d_1(h_1+h_2)}{h_2\lambda_n^3}\right]\exp(\lambda_n x_1) \\ \displaystyle +\frac{1}{2}\left(F_7 + \frac{d_1h_1 - d_2h_2}{h_2}F_{12}\right)x_1^{\,2} + F_{13}x_1 + F_{18}\end{array}\right\}.
\end{aligned}
\tag{A.5}
$$

And lastly, the transverse mid-plane displacements are:

$$
\begin{aligned}
w_1(x_1) &= -\frac{1}{d_1h_1 - d_2h_2}\left\{\begin{array}{l}\displaystyle\sum_{n=1}^{6} F_n\left[\frac{d_1h_1}{k_\sigma} - \frac{d_2h_2c_1 + d_1h_1c_2}{\lambda_n^2} + \frac{d_1d_2(h_1+h_2)}{\lambda_n^4}\right]\exp(\lambda_n x_1) \\ \displaystyle +\frac{1}{6}\left[d_1h_1F_7 - d_1F_9(d_1h_1 - d_2h_2)\right]x_1^{\,3} \\ \displaystyle +\frac{1}{2}d_1h_1F_{10}x_1^{\,2} + \left[d_1h_1F_{15} + c_1F_9(d_1h_1 - d_2h_2)\right]x_1 + F_{16}\end{array}\right\}, \\
w_2(x_1) &= -\frac{1}{d_1h_1 - d_2h_2}\left\{\begin{array}{l}\displaystyle\sum_{n=1}^{6} F_n\left[\frac{d_2h_2}{k_\sigma} - \frac{d_2h_2c_1 + d_1h_1c_2}{\lambda_n^2} + \frac{d_1d_2(h_1+h_2)}{\lambda_n^4}\right]\exp(\lambda_n x_1) \\ \displaystyle +\frac{1}{6}\left[d_2h_2F_7 + d_2F_{12}(d_1h_1 - d_2h_2)\right]x_1^{\,3} \\ \displaystyle +\frac{1}{2}d_2h_2F_{13}x_1^{\,2} + \left[d_2h_2F_{18} - c_2F_{12}(d_1h_1 - d_2h_2)\right]x_1 + F_{19}\end{array}\right\}.
\end{aligned}
\tag{A.6}
$$

Here, F_8, F_9, …, F_{19} are the integration constants to be determined by imposing the boundary and continuity conditions.

A.2. Internal forces and displacements in Region 2

For Region 2, the analytical solutions to the differential Eq.(9) are obtained lightly, yielding the expressions for the mid-plane displacements of the substrate s follows:

$$
\begin{aligned}
u_3^{\circ}(x_2) &= F_{20}x_2 + F_{21}, \\
\phi_3(x_2) &= \frac{1}{2}F_{22}x_2^2 + F_{23}x_2 + F_{24}, \\
w_3(x_2) &= -\frac{1}{6}F_{22}x_2^3 - \frac{1}{2}F_{23}x_2^2 + F_{25}x_2 + F_{26}.
\end{aligned}
\tag{A.7}
$$

By substituting the expressions for the displacements into Eq.(6) and taking the derivative with respect to x_2, the expressions for the internal forces are deduced:

$$\begin{aligned} &N_3(x_2) = A_2 F_{20}, \\ &M_3(x_2) = D_2(F_{22}x_2 + F_{23}), \\ &Q_3(x_2) = C_2(F_{24} + F_{25}). \end{aligned} \tag{A.8}$$

Here, F_{20}, F_{21}, …, F_{26} are further seven integration constants.

A.3. Relations among the integration constants

When the expressions for the adhesive stresses and displacements in Region 1 are introduced into Eq.(4), we can find seven relationships among the constants as follows:

$$\begin{aligned} &F_7 - d_1F_9 - d_2F_{12} = 0, \\ &\left(a_2 + a_1 + d_2h_2^2 + d_1h_1^2\right)F_7 + \left(d_1h_1 - d_2h_2\right)\left(d_2h_2F_{12} - d_1h_1F_9\right) = 0, \\ &a_1F_8 + a_2F_{11} + d_1h_1^2F_{10} + d_2h_2^2F_{13} = 0, \\ &d_1h_1F_{10} - d_2h_2F_{13} = 0, \\ &\left(d_1h_1 - d_2h_2\right)\left(c_1F_9 + c_2F_{12}\right) + d_1h_1F_{15} - d_2h_2F_{18} = 0, \\ &a_1F_{14} + d_1h_1^2F_{15} + a_2F_{17} + d_2h_2^2F_{18} - F_7/k_\tau = 0, \\ &F_{16} - F_{19} = 0. \end{aligned} \tag{A.9}$$

For Region 2, an additional relationship is deduced by substituting the expressions for Q_3 and M_3 into Eq.(6). Namely:

$$D_2F_{22} - C_2\left(F_{24} + F_{25}\right) = 0 \tag{A.10}$$

References

Agrawal, A., Karlsson, A., 2006. Obtaining mode mixity for a bimaterial interface crack using the virtual crack closure technique. Int. J. Fract. 141, 75-98.

Bennati, S., Colleluori, M., Corigliano, D., Valvo, P.S., 2009. An enhanced beam-theory model of the asymmetric double cantilever beam (ADCB) test for composite laminates. Compos. Sci. Technol. 69, 1735-1745.

Camanho, P.P., Davila, C.G., 2002. Mixed-mode decohesion finite elements for the simulation of delamination in composite materials. Technical Report, NASA/Technical Memorandum, TM-2002-211737.

Chadegani, A., Yang, C., Smeltzer, S.S., 2012. Adhesive-Bonded Composite Joints Analysis with Delaminated Surface Ply Using Strain-Energy Release Rate. J. Aircr. 49, 503-520.

Chadegani, A. and Batra, R. C., 2011. Analysis of adhesive-bonded single-lap joint with an

interfacial crack and a void. Int. J. Adhes. Adhes. 31, 455-465.

da Silva, L.F.M., das Neves, P.J.C., Adams, R., Spelt, J., 2009. Analytical models of adhesively bonded joints-Part I: Literature survey. Int. J. Adhes. Adhes. 29, 319-330.

Feng, Y., Wu, L., 2001. Analysis of interfacial thermal stresses of chip-substrate structure. Int. J. Solids Struct. 38, 1551-1562.

Gleich, D., Van Tooren, M., Beukers, A., 2001. Analysis and evaluation of bondline thickness effects on failure load in adhesively bonded structures. J. Adhes. Sci. Technol. 15, 1091-1101.

Goland, M., Reissner, E., 1944. The stresses in cemented joints. J. Appl. Mech.-Trans. ASME 11, A17-A27.

He, M.Y., Evans, A.G., Hutchinson, J.W., 1997. Convergent debonding of films and fibers. Acta Mater. 45, 3481-3489.

Huang, Y., Chen, J., Yin, Z., Xiong, Y., 2011. Roll-to-roll processing of flexible heterogeneous electronics with low interfacial residual stress. IEEE Trans. Compon. Pack. Manuf. Technol. 1, 1368-1377.

Hutchinson, J., Suo, Z., 1992. Mixed mode cracking in layered materials. Adv. Appl. Mech. 29, 63-191.

Ko, H.C., Stoykovich, M.P., Song, J., Malyarchuk, V., Choi, W.M., Yu, C.J., Geddes Iii, J.B., Xiao, J., Wang, S., Huang, Y., 2008. A hemispherical electronic eye camera based on compressible silicon optoelectronics. Nature 454, 748-753.

Krenk, S., 1992. Energy release rate of symmetric adhesive joints. Eng. Fract. Mech. 43, 549-559.

Krueger, R., 2004. Virtual crack closure technique: History, approach, and applications. Appl. Mech. Rev. 57, 109-143.

Li, R., Li, Y., Chaofeng, L., Song, J., Saeidpouraza, R., Fang, B., Zhong, Y., Ferreira, P.M., Rogers, J.A., Huang, Y., 2012. Thermo-mechanical modeling of laser-driven non-contact transfer printing: two-dimensional analysis. Soft Matter 8, 3122-3127.

Li, S., Wang, J., Thouless, M.D., 2004. The effects of shear on delamination in layered materials. J. Mech. Phys. Solids 52, 193-214.

Lu, N., Yoon, J., Suo, Z., 2007. Delamination of stiff islands patterned on stretchable substrates. Int. J. Mater. Res. 98, 717-722.

Luo, Q., Tong, L., 2004. Linear and higher order displacement theories for adhesively bonded lap

joints. Int. J. Solids Struct. 41, 6351-6381.

Luo, Q., Tong, L., 2009. Energy release rates for interlaminar delamination in laminates considering transverse shear effects. Compos. Struct. 89, 235-244.

Park, S., Ahn, J., Feng, X., Wang, S., Huang, Y., Rogers, J., 2008. Theoretical and Experimental Studies of Bending of Inorganic Electronic Materials on Plastic Substrates. Adv. Funct. Mater. 18, 2673-2684.

Peng, B., Huang, Y., Yin, Z., Xiong, Y., 2012. Competing Fracture Modeling of Thin Chip Pick-Up Process. IEEE Trans. Compon. Pack. Manuf. Technol. 2, 1217-1225.

Peng, B., Huang, Y.A., Yin, Z.P., Xiong, Y.L., 2011. Analysis of interfacial peeling in IC chip pick-up process. J. Appl. Phys. 110, 0735081-7.

Qiao, P., Wang, J., 2004. Mechanics and fracture of crack tip deformable bi-material interface. Int. J. Solids Struct. 41, 7423-7444.

Saiki, N., Inaba, K., Kishimoto, K., Seno, H., Ebe, K., 2010. Study on Peeling Behavior in Pick-up Process of IC Chip with Adhesive Tapes. J. Solid Mech. Mater. Eng. 4, 1051-1060.

Shahin, K., Taheri, F., 2008. The strain energy release rates in adhesively bonded balanced and unbalanced specimens and lap joints. Int. J.Solids Struct. 45, 6284-6300.

Tsai, M., Oplinger, D., Morton, J., 1998. Improved theoretical solutions for adhesive lap joints. Int. J. Solids Struct. 35, 1163-1185.

Valvo, P.S., 2012. A revised virtual crack closure technique for physically consistent fracture mode partitioning. Int. J. Fract. 173, 1-20.

Wang, J., Qiao, P., 2004. On the energy release rate and mode mix of delaminated shear deformable composite plates. Int. J. Solids Struct. 41, 2757-2779.

Wang, J., Zhang, C., 2009. Energy release rate and phase angle of delamination in sandwich beams and symmetric adhesively bonded joints. Int. J. Solids Struct. 46, 4409-4418.

Wang, K.P., Huang, Y.Y., Chandra, A., Hu, K.X., 2000. Interfacial shear stress, peeling stress, and die cracking stress in trilayer electronic assemblies. IEEE Trans. Compon. Pack. Manuf. Technol. 23, 309-316.

Xie, D., Biggers, S.B., 2006. Progressive crack growth analysis using interface element based on the virtual crack closure technique. Finite Elem. Anal. Des. 42, 977-984.

Xie, D., Biggers, S.B., 2007. Calculation of transient strain energy release rates under impact

loading based on the virtual crack closure technique. Int. J. Impact Eng. 34, 1047-1060.

Yang, C., Chadegani, A., Tomblin, J.S., 2008. Strain energy release rate determination of prescribed cracks in adhesively-bonded single-lap composite joints with thick bondlines. Compos. Part B: Eng. 39, 863-873.

Yang, C., Pang, S.S., 1996. Stress-strain analysis of single-lap composite joints under tension. J. Eng. Mater. Technol.-Trans. ASME 118, 247-255.

Vitae

Zunxu Liu received the B.S. and M.S. degrees in Mechanical Engineering from Northeastern University, Shenyang, China, in 2009 and 2011, respectively.

He is pursuing the Ph.D. degree in Mechanical Engineering at the School of Mechanical Science and Engineering, Huazhong University of Science and Technology (HUST), Wuhan, China, from 2011. He is also with the State Key Laboratory of Digital Manufacturing Equipment and Technology, HUST.

Paolo S. Valvo graduated with honours in Civil Engineering at the University of Pisa in 1996 and obtained his PhD in Structural Engineering from the University of Florence in 2001. Since 2006

he is Assistant Professor of Structural Mechanics at the University of Pisa. Since 2010 he acts also as Aggregate Professor of Structural Dynamics. His research activities range throughout the field of the Mechanics of Solids and Structures, with particular focus on problems involving Fracture Mechanics, Composite Materials, Stability of Structures, and Computational Mechanics.

YongAn Huang received the B.S. and M.S. degrees in Civil engineering in 2001 and 2004, and Ph.D. degree in Engineering Mechanics in 2007, from Northwestern Polytechnical University, Xi'an, China, respectively.

He was a Postdoctoral Fellow at the School of Mechanical Science and Engineering, HUST, in 2007. He is now an Associate Professor in the State Key Laboratory of Digital Manufacturing Equipment and Technology at HUST. He is principal investigator for projects sponsored by General Program and key Program of National Science Foundation of China. His research interests are focused on flexible electronics manufacturing and advanced material and structural mechanics.

Zhouping Yin received the B.S. and Ph.D. degrees in Mechanical Engineering from HUST, in 1994 and 2000, respectively.

He is a Distinguished Professor and has been Vice Head of the State Key Laboratory of Digital Manufacturing Equipment and Technology, HUST, since 2005. He is awarded the China National

Funds for Distinguished Young Scientists. He is principal investigator for projects sponsored by General Program and Major Program of National Science Foundation, National Basic Research Project of China. He is leading a research group and conducting research in the electronic manufacturing equipment and technology, including printed electronics and RFID packaging.

List of table captions

Table 1 Geometrical dimensions and material properties for the illustrative example.

Layers	Thickness (μm)	Young's modulus (MPa)	Poisson's ratio	Material
Chip	100	129,000	0.28	Silicon
Adhesive	5	20	0.40	Acryl/epoxy resins
Substrate	100	160	0.45	Polyolefin

List of figure captions